Motion Compensation for MRI-Compatible Patient-Mounted Needle Guide Device: Estimation of Targeting Accuracy in MRI-Guided Kidney Cryoablations

Junichi Tokuda[1], **Laurent Chauvin**[1], **Brian Ninni**[1], **Takahisa Kato**[1,2], **Franklin King**[1], **Kemal Tuncali**[1], and **Nobuhiko Hata**[1]

[1]Department of Radiology, Brigham and Womens Hospital and Harvard Medical School, Boston, MA, USA

[2]Healthcare Optics Research Laboratory, Canon U.S.A., Inc., Cambridge, MA, 02139, USA

Abstract

Rationale and Objectives—Patient-mounted needle guide devices for percutaneous ablations are vulnerable to patient motion. The objective of this study is to develop and evaluate a software system for MRI-compatible patient-mounted needle guide device that can adaptively compensate for the displacement of the device due to the patient motion using a novel image-based automatic device-to-image registration.

Materials and Methods—We developed a software system for an MRI-compatible patient-mounted needle guide device for percutaneous ablations. It features fully-automated image-based device-to-image registration to track the device position and a device controller to adjust the needle trajectory to compensate for the displacement of the device. We performed: a) a phantom study using a clinical MR scanner to evaluate the performance of registration, b) simulations using intraoperative time-series MR data acquired in 20 clinical cases of MRI-guided renal cryoablations to assess its impact on motion compensation, and c) pilot clinical study in three patients to test its feasibility during the clinical procedure.

Results—FRE, TRE, and success rate of device-to-image registration were 2.71 ± 2.29 mm, 1.74 ± 1.13 mm, and 98.3% for the phantom images. The simulation study showed that the motion compensation reduced the targeting error for needle placement from 8.2 mm to 5.4 mm ($p < 0.0005$) in patients under general anesthesia (GA), and from 14.4 mm to 10.0 mm ($p < 1.0 \times 10^{-5}$) in patients under monitored anesthesia care (MAC). The pilot study showed that the software registered the device successfully during clinical cases.

Discussion and Conclusion—Our simulation study demonstrated that the software system could significantly improve the targeting accuracy both in patients treated under MAC and GA. Intra-procedural image-based device-to-image registration was feasible.

1. Introduction

Image-guided percutaneous tumor ablations are widely practiced to treat liver and kidney cancers. Several ablation modalities are clinically available, including cryoablation [1–3], radiofrequency ablation (RFA) [4, 5], microwave ablations (MWA) [6–8], laser ablations [9], and irreversible electroporation (IRE) [10]. While ultrasound and computed tomography (CT) are common imaging modality of choice for guiding ablation applicator needles into the target lesion and monitoring the therapeutic effect [1, 11], magnetic resonance imaging (MRI) is preferable when the tumor does not present distinctive contrast against the surrounding tissue in other modalities [2, 3]. Intraprocedural MRI can provide high-resolution 2- or 3-dimensional images with superior soft tissue contrast without exposing the patient and clinical staff to ionizing radiation. MRI also offers unique capabilities in monitoring the ablation zone; it can visualize formation of the ice ball as a signal void in cryoablations [2] or temperature variations in heat-based thermal ablations [12]. Intraprocedural MRI helps physicians ensure sufficient ablation margins while avoiding damage to critical structures; hence, it potentially leads to the reduction of tumor recurrence and post-procedural complications.

One technical challenge of MRI-guided ablation is that the narrow MRI gantry hampers the placement of ablation needles during imaging. Therefore, patient needs to be moved into the gantry for imaging and out for needle placement [2]. This "in/scan-out/adjust" technique [2] inhibits the physicians from interactively maneuvering the needles while visually monitoring the needle location relative to the target on the image. Typically, a repeated in/scan-out/adjust process is required until the needle reaches the intended location, leading to prolonged procedure time, unlike other imaging modalities such as ultrasound and CT fluoroscopy. There have also been attempts to maneuver the needle inside the closed-bore scanner for interactive real-time MR image guidance [13]. However, this requires the physician to reach the needle near the isocenter from the bore entry, which is ergonomically challenging; the distance between the bore entrance and the isocenter is 60–70 cm even in a state-of-the-art short-bore scanner. While open-configuration scanners have been investigated to address this challenge [14–17], they have not become a mainstream because of the limited imaging capability compared to the conventional closed-bore scanners [18].

A needle guide device, which mechanically guides a needle to a pre-defined target, can potentially make the "in/scan-out/adjust" process less cumbersome. Such a device physically assists the physician to direct the needle to the target; hence, it would reduce the number of "in/scan-out/adjust" steps. Needle guide devices can be categorized as either table-, gantry-, and floor-mounted systems [19–22] or patient-mounted systems [23–25] based on how the devices are fixed [26]. A patient-mounted system is directly attached to the patients skin rather than the floor or the patient table, and thus one can hypothesize that it is relatively easier to maintain the relationship between the needle guide and the target lesion, and is less vulnerable to the patient motion.

While previous studies [24, 25] have successfully demonstrated the feasibility of the patient-mounted systems, two important questions have yet to be answered: how the patient motion impacts the needle placement accuracy, and how such motion can be managed. In the

clinical scenario, the patient motion comprises the motion of the body surface and the internal organ, which can move independently, and causes significant displacements of the device with respect to the target lesion. Given that imaging and needle placement take place at different time points in the procedure, it is important to estimate potential targeting accuracy due to the motions of the body surface and the internal organ. Although our previous study using a phantom [25] has shown that the patient-mounted needle guide device provided better probe placement accuracy than manual procedure, even in the presence of random patient motion, the study only considered a rigid patient motion, where the body surface and the target in the internal organ move together. In the clinical scenario, the patient motion is induced by the deformation of the chest and abdominal areas, and thus the spatial relationship between the device and the target is constantly changing throughout the procedure.

In this study, we newly developed a software system for an MRI-compatible patient-mounted needle guide device developed in our previous work [25] with an emphasis on a novel automatic device-to-image registration algorithm. Our hypothesis is that the algorithm would enable re-registering the patient-mounted device after each image acquisition continuously; hence it would correct for the misalignment between the needle guide and the target that accumulates over the course of the repeated in/scan-out/adjust process due to the drift of the patient and the internal organ. This new capability of continuous re-registration would help reducing the targeting error. Therefore, the objective of this study is three-fold: 1) to evaluate the performance of the proposed registration algorithm in phantom, 2) to estimate the impact of the motion compensation in the clinical scenario using a simulation with clinical images, and 3) to test feasibility of the proposed registration algorithm in patients.

2. Materials and Methods

2.1. MRI-compatible Patient-Mounted Needle Guide Device

The MRI-compatible patient-mounted needle guide device used in this study is equipped with a double-ring mechanism presented previously [25] (Figure 1). This active 2-DoF mechanism tilts a passive needle guide about the remote center of motion (RCM) to guide a biopsy or ablation needle to the target localized on an intraprocedural MR image. The device is placed on the surface of the patients body so the RCM is aligned with the needle entry point on the skin, and is then fixed with straps. The 2-DoF RCM motion is achieved by a double-ring mechanism, which consists of two ring-shape rotary stages coupled with a fixed angle. Those stages are driven by custom-made ultrasonic actuators with embedded encoders (Figure 1). Advantages of this unique double-ring mechanism include: 1) a wide access to the skin entry point for the physician; 2) ring-shape rotary stages, which are suitable to house the ultrasonic actuators and rotary encoders; 3) a rigid structure with small footprint; 4) a simple and safe mechanism with a low risk of catching clinicians fingers, patients skin, drapes, blankets, or other equipment.

MR-visible spherical fiducial markers are embedded in the device in order to localize the device on the image and register it to the image coordinate system. A fully-automated algorithm to detect and register the fiducial markers, which is the new contribution of this

study, is described in the Fully-Automated Fiducial-Based Device-to-Image Registration section.

2.2. Overview of Software System

We developed navigation software specifically for the MRI-compatible patient-mounted needle guide device. Our system consists of navigation software and a needle guide device controller running as separate processes. They exchange messages such as commands, device statuses, and target locations during a procedure using the OpenIGTLink network communication protocol [27]. The navigation software can also import intraprocedural MR images immediately after the acquisition through the local area network in the operating room using the Digital Imaging and Communications in Medicine (DICOM) standard [28].

The navigation software works as a primary user interface for the physician and operator. It is implemented as a plug-in module for 3D Slicer, open-source medical image computing software, [29,30]. In addition, the plug-in module provides features to support the clinical workflow described in the next section, including needle insertion planning, device-to-image registration, device control and monitoring, and needle placement monitoring.

The controller is in charge of controlling the actuators and monitoring the encoders and sensors. The controller receives control commands and parameters (e.g. registration transform and target coordinates) and sends hardware status (e.g. current orientation of the needle guide, and hardware error information) from and to the navigation software. The received target coordinates are translated to displacements of individual actuators by computing the inverse kinematics, and passed to the PID control to control individual actuators. The encoder readings are converted to the orientation of the needle guide and sent back to the navigation software.

2.3. Clinical Workflow With and Without Motion Compensation

We consider the clinical workflow shown in Figure 2 to introduce ablation needles into the target lesion under MRI guidance. The workflow is based on the "in/scan-out/adjust" approach; the patient stays on the patient table throughout the procedure, and is moved into the scanners gantry only when images are acquired; the other steps are performed outside the gantry. The workflow consists of Planning, Device-to-Image Registration, Device Control, and Needle Placement steps (Figure 2).

1. **Planning.** The physician defines needle insertion trajectories by specifying target and skin entry points on a 3D MR image of the patient (*planning image*). The physician can review the trajectories by re-slicing the 3D image at any plane along the trajectory and ensure that there is no critical structure and/or obstacle around it.

2. **Device-to-Image Registration.** The navigation software registers the needle guide device to the image coordinate system by detecting a fiducial frame attached to the device on intraoperative images (*registration image*). The detail of the algorithm is described in the following section. Once the device has been registered, the physician can confirm that all targets are within the targeting

range of the device on the image. The result of the registration is transferred to the controller over the network using the OpenIGTLink protocol [27].

3.   **Device Control.** The navigation software sends the coordinates of the current target to the device controller over the network using the OpenIGTLink protocol. It also displays information necessary for the physician to place the needles, including insertion depth.

4.   **Needle Placement Monitoring.** The physician can check the placement of the needle visually by comparing an image acquired after placing the needles (*confirmation image*) and the planned trajectory. The confirmation image can also be used to re-register the device to the new patient location.

Typically, a registration image is acquired only once as part of the planning unless the patient position is significantly changed during the procedure. However, if the field of view of the confirmation image is large enough to cover the fiducial markers embedded in the device, the device could be re-registered to the most recent confirmation image (indicated as broken lines in Figure 2). This re-registration process would keep updating the needle placement to reflect the current position and orientation of the device; hence, it would compensate for the displacement of the device due to the patient motion. To use this motion compensation technique in practice, a robust, fast, and automated registration process is crucial. We developed a new fiducial-based device-to-image registration algorithm to achieve this goal.

2.4. Fully-Automated Fiducial-Based Device-to-Image Registration

2.4.1. Configuration of fiducial frame—The device-to-image registration was achieved by detecting an MR-visible fiducial frame attached to the device in an MR image and registering the fiducial frame model to the detected frame. The challenge in this approach is that the markers on the MR image must be identified correctly regardless of the presence of other objects in the field of view, such as part of the patient's body. We developed a fiducial frame that consisted of multiple MR-visible spherical markers aligned in a circular configuration and an algorithm to detect and register the developed fiducial frame. Our algorithm relies on a spherical shaped marker with a specific diameter d_M, and the circular configuration of those markers (Figure 3). Spherical markers were used because spherical objects on an image can be detected by means of image processing regardless of orientation, and they are easily fabricated. We used 3D-printed spherical liquid container with a radius of 10 mm filled with Gd-DTPA solution. The circular configuration is suited for the double-ring mechanism [25]. The spherical markers are aligned in the circular configuration and spaced irregularly so that the configuration is asymmetric, giving a unique solution for the registration. In this study, eight markers were aligned on a ring with a diameter of 92 mm. The angles between the markers were 51.43°, 41.14°, 56.57°, 61.71°, 20.57°, 30.86°, 61.71°, and 36.00°. The radius of the device was constrained by the diameter of the MR loop coil used for the procedure.

2.4.2. Detection of Spherical Markers—The detection of spherical markers consists of two steps. The first step in the detection of the spherical markers is enhancing spherical objects using a filter proposed by Frangi *et al* [31]. We configured the parameters to enhance

bright spherical markers on the image. The enhanced objects were then detected by Hough transform [32]. We used implementations of those algorithms available for the Insight Segmentation and Registration Toolkit (ITK) [33, 34]. The endpoint of this step is the position of the center of mass for each spherical object (Figure 3(b)).

2.4.3. Registration of Fiducial Marker Model to Detected Fiducial Markers—The last step is matching the model of markers to the detected markers. This step consists of five sub-steps: 1) fit a 2-dimensional plane to the detected markers (Figure 3(c)); 2) estimate the circle, which the detected markers are aligned to (Figure 3(d)); 3) detect and remove outlying markers; 4) match the model circle to the estimated circle (Figure 3(e)); 5) find the rotation that matches the model and detected markers (Figure 3(f)). The first sub-step is achieved using a principal component analysis (PCA). Given the coordinates of the detected markers $X = (x_1, x_2, \ldots, x_N)$, the principal component decomposition can be given using a 3-by-3 matrix W as:

$$T = \hat{X}W, \quad (1)$$

where T is an N-by-3 matrix representing the coordinates of the markers converted to the new coordinate system, $\hat{X}$ is an N-by-3 matrix representing the coordinates of the markers shifted so that the empirical mean is zero ($\hat{X} = (x_1 - \bar{x}, x_2 - \bar{x}, \ldots, x_N - \bar{x})$, where $\bar{x} = \sum_{n=1}^{N} x_n/N$). The all markers are in the plane defined by the first and the second axes, if marker detection errors are ignorable.

In the second sub-step, the center of the markers is estimated by the intersection of the perpendicular bisectors of two chords defined by three different points on the circle (see Appendix). In our implementation, the bisectors calculated from all $\binom{N}{3}$ combinations of points are averaged to estimate the center of the markers.

In the third sub-step, objects that have been falsely detected due to image noises or spherical objects are filtered out recursively based on: 1) the error between the distance from the estimated center of the circle and the known radius of the circle (radius error), 2) the error from the estimated plane of the circle (out-of-plane error), and 3) the error between the distance from a pseudo center estimated from other three detected objects and the known radius of the circle (cross-validation radius error).

In the forth sub-step, the transformation that fits the circle in the model to the detected markers is:

$$T_{C+}(p) = R_{C+}p + c, \quad (2)$$

where $R_+ = (w_1^T, w_2^T, w_3^T)$, and where p is the coordinates of the fiducial marker in the model. The circle can also be fitted to the model, after flipping (or rotating about x- or y- axis by 180 degrees). In this case, the transformation is:

$$T_{C\,-}(p) = R_{C\,-}p + c = R_{C\,+}R_{x,\,180°}p + c, \quad (3)$$

where $R_{x,180°}$ is a counter-clockwise rotation about the x-axis by 180 degrees.

The last sub-step is finding the rotation about the axis of the circle that fits the all model markers to the detected markers after transformation T_{c+} or T_{c-}. Given an angle for the rotation about the z-axis θ, the final transformation can be described as:

$$T_\theta(p) = R_C R_z(\theta)p + c . \quad (4)$$

We define a goodness of fit as the mean square distance of closest points between the transformed model markers and the detected markers as:

$$E = \frac{1}{N}\sum_{k=1}^{N} \min_j \|q_j - T_\theta(p_k)\|^2. \quad (5)$$

where p_i is the coordinates of the i-th fiducial marker in the model, and q_j is the coordinates of the i-th fiducial marker detected on the image. Using this goodness of fit, our problem can be described as:

$$\theta = \arg\min_\theta E = \arg\min_\theta \frac{1}{N}\sum_{k=1}^{N} \min_{j\in 1,\ldots,N} \|q_j - T_\theta(p_k)\|^2. \quad (6)$$

Finally, the registration transform can be computed by substituting the solution θ to $T_\theta(p)$.

3. Experiments

3.1. Validation of Device-to-Image Registration using MR images of Fiducial Markers

We performed an imaging experiment in a 3-Tesla wide-bore MRI scanner (MAGNETOM Verio, Siemens Healthcare, Erlangen, Germany) with a Body Matrix coil. The goal of this experiment is two-fold: 1) to determine the realistic accuracy of the proposed device-to-image registration in the presence of field inhomogeneity; 2) to compare the performance with a conventional fiducial-based registration. We built a platform to place the fiducial frame at known location with respect to the isocenter of the scanner. The platform consists of a base table and jigs to fix the fiducial frame to the table at discrete position and orientation. The base table was manually aligned to the alignment laser of the scanner so that the fiducial frame was approximately at the isocenter with the circular plane parallel to the patient table. Coordinates were noted in the same way as the patient coordinate system in the supine/feet-first position; the axis of the gantry corresponded to the superior-inferior (S-I) axis, the vertical and horizontal axes in the cross section of the gantry corresponded to the anterior-posterior (A-P) and right-left (R-L) axes respectively.

The fiducial frame was discretely translated or rotated by adding or replacing the jigs; it was translated by 0, 50, 100, and 150 mm from the isocenter along the R-L and S-I axes, and 0, 10, 20, 30, and 40 mm along the A-P axis; it was rotated from its initial orientation by 0°, 15°, 30°, 45°, 75°, and 90°about the R-L and S-I axes, and 0°, 90°, 180°, and 270°about the A-P axis. We had a limited translation range in the A-P direction, because we needed to cover the entire jigs with the Body Matrix coil to use the same imaging setup as our clinical application.

At each position and orientation, a multi-slice MR image of the fiducial frame was acquired in the coronal plane using a T2-weighted Half-Fourier Acquisition Single-shot Turbo spin Echo (HASTE) sequence (TR/TE: 1000/198 ms; flip angle: 131°; pixel size: $1.09375 \times 1.09375 mm^2$; FOV: $300 \times 255 mm^2$; bandwidth: 504 Hz/pixel; slice thickness: 2mm; number of slices: 19–80), which has been used for MRI-guided cryoablation of the kidney and liver at our institution.

After all images were acquired, the translation and rotation of the fiducial frame from its initial position were estimated from the images using the proposed automatic device-to-image registration. The result was compared with reference translation and rotation calculated based on the configuration of the jigs to calculate the registration error. The experiment was repeated for twenty times. Registration errors were evaluated as fiducial registration error (FRE), and target registration error (TRE). We assumed that the target was on the axis of the base ring (or the circular fiducial frame), and the distance between the target and the fiducial frame was 150mm, which is approximately the maximum distance for the needle guide device with a 175-mm needle.

In addition, the translation and rotation of the fiducial frame were also estimated using the conventional fiducial-based registration. In this approach, the center of each fiducial marker was localized manually with the mouse cursor and recorded. The model of the fiducial frame was registered to the image by matching the coordinates of individual markers in the model to those localized on the image using the Fiducial Registration module in 3D Slicer. Like the evaluation of the automatic registration, the registration error was calculated based on the reference translation and rotation. The registration errors for the automatic registration and those for the manual registration were then compared using a *t*-test.

3.2. Simulation of Targeting Error Due to Patient Motion During MRI-guided Kidney Ablations

This retrospective image analysis study was approved by the institutional review board at Brigham and Womens Hospital (BWH) and was HIPAA-compliant. The goal of the study is to estimate possible targeting errors with the patient-mounted needle guide due to patient motion during the procedure, and estimate how the motion compensation with the proposed automatic device-to-image registration could potentially suppress such errors. Our hypothesis is that the fully automated registration would make it feasible to counteract the patient motion by re-registering the device to every confirmation images (Figure 2), which are acquired to check the needle location after every insertion. Repeated re-registration would allow updating the needle placement plan adaptively even if the device is displaced by the motions of the body surface.

3.2.1. Subjects—The inclusion criteria were subjects who had confirmed renal tumor and underwent MRI-guided kidney cryoablations performed by one radiologist (K.T.) between May 2013 and August 2014. Using these criteria, 20 subjects (ages 46–87 years; 6 males and 14 females) were included in the study. Tumor ablations were conducted using cryoablation (Galil Medical Ltd., Yokneam, Israel). The patients were treated under either general anesthesia (GA) ($N = 8$) or monitored anesthesia care (MAC) ($N = 12$).

3.2.2. Imaging Protocol—All intraoperative images were acquired using the same scanner as the imaging study for the validation of the device-to-image registration. Multislice T2-weighted MR images were acquired during the needle placement process using the same Body Matrix coil and the multi-slice T2-weighted HASTE sequence (TR/TE: 1000/200 ms; flip angle: 129 – 147°; acquisition matrix: 320 × 190; FOV: 289×340; bandwidth: 504 Hz/pixel, slice thickness: 4mm; number of slices: 8–20). MR imaging was performed during controlled apnea for the cases with GA, or breath-hold for the cases with MAC.

3.2.3. Simulation of device displacement due to body surface—The schematic representation of simulation workflow is shown in Figure 4. We virtually mounted the device on a 3D model of the body surface reconstructed from the time series of the intraoperative images. The body of the patient was segmented by applying threshold to each image, and then converted to a surface model using the marching cube method [35] available on 3D Slicer. The entry point of the needle on the skin was also identified based on the needle artifact on each image. We assume that the device is placed so that the remote-center-of-motion is aligned to the entry point on the skin in the clinical scenario. Therefore, the position of the virtually-mounted device was determined by matching the remote-center-of-motion with the entry point. Likewise, the orientation of the device was estimated by the average orientation of the polygons in the area on the body surface that would support the base of the device. The area is determined as a circular area around the entry point on the skin surface with the same radius of the base of the device. Based on these position and orientation of the device, we rendered spherical markers of the fiducial frame on each intraoperative image. This "simulated image" mimics intraoperative image of the patient with the patient-mounted needle guide device. We computed the position and orientation of the device for each intraoperative image, and generated simulated images.

3.2.4. Assessment of target organ displacement—Displacements of the kidney were estimated by registering the first frame of the series to that in the subsequent frames. An intensity-based rigid registration with maximization of mutual information implemented in the BRAINSFit module of 3D Slicer [36] was used. To register only the kidney, it was roughly contoured on the image manually to mask the area outside the kidney. The registration was visually confirmed. The translation of the kidney was then applied to the initial position of the target to obtain the positions of the target at each frame.

3.2.5. Simulation of needle placement with and without re-registration of the needle guide device—Using the data obtained in sections 3.2.1–3.2.4, we simulated

target planning, fiducial registration, and needle placement using the simulated images and evaluated potential needle placement errors. We consider the following two scenarios:

Needle placement without re-registration This is a conventional scenario, where a plan is made only once at the beginning and never updated throughout the procedure (Figure 4(a)). First, a target was defined in the kidney tumor on the first frame of the simulated images. The needle guide device was registered to the simulated image using the device-to-image registration method. The needle guide angle was determined based on the target position and the registration of the device. A needle was then virtually placed on the i-th simulated image using the planned needle guide angle. We assumed that the needle guide maintained its angle, but was displaced due to the body surface displacement. Therefore, the resulted needle trajectory on the i-th simulated image was determined by transforming the device to the position and orientation of the device on the i-th image. Likewise, we assumed that the target in the kidney was displaced due to the motion of the kidney, and the target position on the i-th image was estimated by applying the transform of the kidney to the original target. Finally, the distance between the resultant trajectory and the target was measured as an expected targeting error (ETE).

Needle placement with re-registration This is a scenario enabled by our automatic device-to-image registration technique; the needle guide was re-registered to each simulated image, and therefore the plan was kept up to date (Figure 4(b)). The needle guide angles were then updated before simulating the next simulated image. The resultant needle trajectory on the i-th simulated image was determined by transforming the device with the needle guide angle updated for $(i-1)$-th simulated image to the position and orientation of the device on the i-th image. Finally, the distance between the trajectory and the target was measured as ETE. The ETEs for both scenarios were then statistically compared using a paired Wilcoxon rank sum test.

3.3. Pilot Clinical Study During MRI-Guided Kidney Ablations

This clinical study was approved separately by the institutional review board at BWH and was HIPPA-compliant. We performed a pilot study to demonstrate the feasibility of the proposed device-to-image registration by acquiring MR image of the fiducial markers embedded in the needle guide device mounted on the actual patient. The study was performed at the beginning of a routine MRI-guided kidney cryoablation procedure; the device was removed before the actual ablation procedure, and thus it was not used for guiding cryoprobes.

3.3.1. Subjects—Subjects were recruited among patients who were scheduled for an MRI-guided renal cryoablation procedure between October and November 2016. Three subjects (ages 58–93; two males and one female) were enrolled.

3.3.2. Imaging, device-to-image registration, targeting, and confirmation—All images were acquired using the same scanner as the previous experiments. A multislice T2-weighted MR registration image was acquired after placing the device on the patient using

the same parameters as the previous experiment. The all patients were under general anesthesia. Images were then transferred to the navigation software over the network. The device-to-image registration was performed as soon as the image was loaded on the navigation software. The image was also assessed by the radiologist to identify the target. Based on the registration and the identified target, the orientation of the needle guide was physically aligned using the actuators. Once the needle guide reached the target orientation, a confirmation image was acquired using the same imaging protocol. To visualize the trajectory of the needle guide on the MR image, a cylindrical fiducial marker was attached along the needle guide.

3.3.3. Validation—Success of device-to-image registration was confirmed by the FRE and by visually comparing the registered fiducial marker model and the registration image. In addition, the ETE was evaluated by comparing the planned target and the trajectory of the needle guide. To visualize the trajectory of the needle guide on the MR image for the evaluation of ETE, a cylindrical fiducial marker with diameter of 8 mm and height of 48 mm was attached along the needle guide.

4. Results

4.1. Validation of Device-to-Image Registration using MR images of Fiducial Markers

The automatic device-to-image registration was successfully performed except for scans where the fiducial frame was displaced by 150 mm from the isocenter in the R direction; in those scans, part of the fiducial frame was not visible due to the limited imaging volume of the scanner, although the entire frame was within the field of view. The overall fiducial detection rate for all scans except for the out-of-range scans was 98.3%, while the processing time was 4.96 ± 1.19 s/image (mean ± SD). Relationship between the translational and rotational parameters and FRE/TRE are shown in Figure 5. The overall FRE and TRE for 150 mm needle insertion were 2.71 ± 2.29 mm and 1.74 ± 1.13 mm (mean ± SD) respectively. Both FRE and TRE increased as the fiducial frame was translated to off-isocenter along the R- and S- axes (Figure 5A and C). FRE and TRE did not increase along A-axis in the range of 20–40 mm (Figure 5B). FRE and TRE also increased as the fiducial frame was rotated about the R- and S- axes from the original position (Figure 5A and C), but not about the A-axis (Figure 5B).

The manual fiducial-based registration was also successfully performed using the same MR image dataset. The average time for the user to identify the markers on the images was 122 seconds. The overall FRE and TRE for 150 mm needle insertion were 2.20 ± 7.98 mm and 2.85 ± 2.94 mm respectively. The overall TRE of the automatic registration was significantly smaller than that of the manual registration ($p < 1.0 \times 10^{-11}$), while there was no significant difference in overall FRE ($p = 0.29$).

4.2. Simulation of Targeting Error Due to Patient Motion During MRI-guided Kidney Ablations

One hundred and ninety-eight images were acquired, and used for the analysis. One hundred and sixty-three images were additionally acquired using a different orientation and/or

sequence to further check the probe locations; however, they were excluded from the study, since they did not sufficiently cover the body surface for estimating the virtual device position. The average interval between two successive image acquisitions for the GA and MAC cases were 4.8 and 4.5 minutes respectively; however, as noted above, some images were acquired in addition to the regular guidance images, and hence those intervals do not necessarily represent the cycle of the in/scan-out/adjust process.

A representative result of automatic re-registration is shown in Figure 6. Among 198 needle confirmation images, the automatic registration software successfully detected and registered the fiducial markers in 193 images (97.5%). The FRE was 1.03 ± 0.36 mm (mean $\pm$ SD). The impact of re-registration to ETE is demonstrated in Figure 7. Reregistration of device at each needle confirmation image significantly improved the ETE from 11.8 mm to 8.1 mm (mean) for the entire patient population ($p < 1.0 \times 10^{-8}$). The re-registration improved the ETE in the both patient groups; the ETE in the patients treated under GA was improved from 8.2 mm to 5.4 mm (mean) ($p < 0.0005$), whereas the ETE in the patients treated under MAC was improved from 14.4 mm to 10.0 mm (mean) ($p < 1.0 \times 10^{-5}$).

4.3. Pilot Study on Patients During MRI-guided Kidney Ablations

Nine registration images and six confirmation images were acquired during the study. When all the markers were shown clearly on the images (4/9 or 44%), all the fiducial markers were detected successfully. In the rest of the images (5/9, or 56%), some of the fiducial markers were not clearly visible or presented in poor quality, resulting in misdetection of those markers. In the latter case, the missing fiducial markers were manually identified by the operator as part of the mitigation plan in the protocol. After fiducial detection, the device-to-image registrations was successfully performed on the all images (100%). The average FRE for the registration was 2.63 mm while the average ETE estimated from the six confirmation images was 8.16 mm. Representative results of the device-to-image registration are shown in Figure 8.

5. Discussion

Patient motion has been a major issue for image-guided percutaneous interventions in abdominal organs. While patient-mounted needle guide systems may help reduce the impact of patient motion by moving with the surface of patient body, few studies have either analyzed such effect quantitatively or suggested how to address them in the workflow aspect. In this study, we presented a new fully-automated device-to-image registration algorithm that only relies on spherical markers with circular configuration, and estimated the potential targeting error by simulating planning and needle insertion using intraprocedural MR images acquired clinically during cryoablations.

There have been several approaches to estimating the patient motion during thermal ablations using additional imaging scanners or sensors including ultrasound imaging [37], surrogate sensors [38], and ultrasound sensors [39]. Those approaches enable compensation of the patient motion with a temporal resolution higher than the MR scan. The use of additional sensors, however, imposes its own engineering and clinical challenges. First, the sensors need to be compatible with the magnetic and RF fields of the MR scanner so that

both the sensors and the scanners work properly without interference. Second, to take full advantage of the high-temporal-resolution tracking, the sensory input must be taken into account in the needle insertion control, which is hard to achieve either manually or robotically, given the frequency of the motion. Our study is rather focused on the inter-scan displacement of the patient body and the device. The method provides a practical solution to minimize the discrepancy between the plan and the actual body configuration.

The study demonstrated that the algorithm detected and registered the fiducial frame robustly with a success rate of 98.3% in the phantom images, and 97.5% in the simulated images with patient body. The algorithm outperformed the conventional fiducial-based registration in terms of TRE, and significantly shortened the time required for the registration process by eliminating the need for manual identification of the markers on the MR images.

There are several findings in the phantom study. First, it proved that the algorithm successfully detected and registered the fiducial frame in the presence of field inhomogeneity and intensity bias due to the coil sensitivity. The study also showed that TRE/FRE depended on the location of the fiducial frame in the actual MRI scanner, due to the inhomogeneity of the magnetic field (Figure 5). In practice, the degradation of FRE/TRE due to the offset along the S-I direction is less concerned than the offsets in the other directions, because the MRI scanner can adjusts the table position to bring the center of imaging volume to the isocenter. The rotation about the A-P axis did not affect the FRE/TRE because the axis of the circular Frame was aligned to the A-P axis. We could not use the same translation range for the translation along the A-P axis, due to the coil configuration.

The simulation study successfully demonstrated the significant improvement of the needle placement accuracy over the course of the repeated in/scan-out/adjust process. The proposed method would have a major clinical impact, because the improved accuracy would reduce the need for re-insertions to adjust the probe positions or additional probes to ensure the tumor coverage. The reduced number of probe insertions could lead to less damage to the patient as well as shorter procedure times.

The pilot study demonstrated that the proposed device-to-image registration was feasible in the clinical setting. The results are still preliminary, and further evaluation is required to determine the robustness of the algorithm. One challenge we found during the study was to acquire a registration image with adequate coverage and signal intensity from the markers; Images with inadequate coverage or signal intensity caused misdetection of the markers. In the future, this could be addressed by scaling down the fiducial frame, because the smaller footprint would make it easier to fit the frame into the imaging volume as well as the sensitive range of the MR coil. The registration algorithm could also be improved by additional validation of detected markers and discarding of invalid markers; the markers can still be matched with the image even if there are few missing markers.

The simulation study using the clinical images and the pilot study provide complementary information. While our pilot study allowed us to evaluate the feasibility of the device and helped identifying the practical issues, the data acquired during the study still did not fully

represent the actual motion of the patient during the ablation. The simulation study, on the other hand, assessed the images obtained during the ablation, and hence it allowed us to estimate potential needle placement accuracies in the presence of patient motion.

The study has three important contributions. First, it proposed a new image-based automatic device-to-image registration algorithm. The configuration of the fiducial frame only requires spherical markers aligned in a circle, and thus can be easily implemented in a wide range of image-guidance applications. While fiducial markers have been used routinely in the clinical practice, robust automatic detection of passive spherical markers is not easily achieved in MR images, because of the inconsistency of signal intensities. Krieger *et al* used two approaches including passive and active fiducial tracking in their MR-compatible needle-guide manipulator noting that segmentation of markers for passive tracking is very time consuming [40]. Active tracking provides faster and more robust registration, though it requires specialized hardware specifically designed for the scanner. Oliveira *et al* proposed phase-only cross-correlation (POCC) algorithm [41], which combines the automatic detection of a passive marker and adjustment of the scan plane to track the needle guide device; the approach still requires a specialized MR pulse sequence. The advantage of our approach is that it does not depend on any specialized hardware or MR pulse sequence, and thus can be easily adapted to any MR hardware. Second, it proposed a computational method to simulate the needle placement workflow, including the device placement, device-to-image registration, and targeting in the presence of patient motion. The method is unique because it considers not only the displacement of the target in the organ, but also the displacement of the body surface. The method would also allow physicians estimating a possible range of needle placement errors if they can manage to acquire a few series of images showing the regular motion of the organ and the body surface. Third, the study has shown that the ability to localize the needle guide device allowed us to keep updating the plan based on the confirmation image for previous needle placement and significantly improved the needle placement accuracy. The study demonstrated the improvement in both the patients under general anesthesia (controlled breathing) and under MAC (free breathing).

There are limitations for our approach. While the coplanar configuration of our fiducial frame can be easily fitted into a patient-mount device such as ours, the registration accuracy depends on the orientation of the frame with respect to the imaging plane as demonstrated in Figure 5. Additional fiducial markers outside the plane would improve the consistency of registration accuracy. In addition, our approach only estimates the rigid transformation of the device; while the simulation study demonstrated that it significantly improved the estimated targeting accuracy, it would not address the targeting error due to the deformation of the patient body. The proposed simulation method does not account for displacement of the body surface and the target organ due to the weight of the device or the interaction with the physician. There are also limitations in our experimental methods. In the simulation study, the slice thickness was larger than the phantom study, because images with the same slice thickness were not available in the clinical data. However, the result shows that our registration method still provided satisfactory registration accuracy.

6. Conclusion

We developed a software system for a MRI-compatible patient-mounted needle guide device, which incorporates a novel automatic device-to-image registration algorithm that allows keeping the device registered to the patient at every image acquisition automatically. Our simulation study using intraprocedural MRI data obtained during clinical MRI-guided cryoablation demonstrated that the automatic registration enabled re-registration of the device, and significantly improved the targeting accuracy both in patients treated under MAC and GA. The pilot clinical study demonstrated that intra-procedural image-based device-to-image registration was feasible.

Acknowledgments

References

1. Orlacchio, Antonio, Bazzocchi, Gabriele, Pastorelli, Daniela, Bolacchi, Francesca, Angelico, Mario, Almerighi, Cristiana, Masala, Salvatore, Simonetti, Giovanni. Percutaneous cryoablation of small hepatocellular carcinoma with US guidance and CT monitoring: initial experience. Cardiovascular and interventional radiology. 2008; 31(3):587–94. [PubMed: 18236104]

2. Morrison, Paul R., Silverman, Stuart G., Tuncali, Kemal, Tatli, Servet. MRI-guided cryotherapy. Journal of magnetic resonance imaging: JMRI. Feb; 2008 27(2):410–20. [PubMed: 18219676]

3. Shimizu, Tadashi, Sakuhara, Yusuke, Abo, Daisuke, Hasegawa, Yu, Kodama, Yoshihisa, Endo, Hideho, Shirato, Hiroki, Miyasaka, Kazuo. Outcome of MR-guided percutaneous cryoablation for hepatocellular carcinoma. Journal of hepato-biliary-pancreatic surgery. Jan; 2009 16(6):816–23. [PubMed: 19466377]

4. McGahan JP, Browning PD, Brock JM, Tesluk H. Hepatic ablation using radiofrequency electrocautery. Investigative radiology. Mar; 1990 25(3):267–70. [PubMed: 2185179]

5. Psutka, Sarah P., Feldman, Adam S., Scott McDougal, W., McGovern, Francis J., Mueller, Peter, Gervais, Debra A. Long-term oncologic outcomes after radiofrequency ablation for T1 renal cell carcinoma. European urology. Mar; 2013 63(3):486–92. [PubMed: 22959191]

6. Seki T, Wakabayashi M, Nakagawa T, Itho T, Shiro T, Kunieda K, Sato M, Uchiyama S, Inoue K. Ultrasonically guided percutaneous microwave coagulation therapy for small hepatocellular carcinoma. Cancer. Aug; 1994 74(3):817–25. [PubMed: 8039109]

7. Morikawa, Shigehiro, Inubushi, Toshiro, Kurumi, Yoshimasa, Naka, Shigeyuki, Sato, Koichiro, Tani, Tohru, Yamamoto, Ikuo, Fujimura, Masaki. MR-guided microwave thermocoagulation therapy of liver tumors: initial clinical experiences using a 0.5 T open MR system. Journal of magnetic resonance imaging: JMRI. Nov; 2002 16(5):576–83. [PubMed: 12412035]

8. Clark, Peter E., Woodruff, Ralph D., Zagoria, Ronald J., Craig Hall, M. Microwave ablation of renal parenchymal tumors before nephrectomy: phase I study. AJR American journal of roentgenology. May; 2007 188(5):1212–4. [PubMed: 17449761]

9. Veenendaal, Liesbeth M., de Jager, Arjan, Stapper, Gerard, Borel Rinkes, Inne HM., van Hillegersberg, Richard. Multiple fiber laser-induced thermotherapy for ablation of large intrahepatic tumors. Photomedicine and laser surgery. Feb; 2006 24(1):3–9. [PubMed: 16503781]

10. Lee, Edward W., Chen, Christine, Prieto, Veronica E., Dry, Sarah M., Loh, Christopher T., Kee, Stephen T. Advanced hepatic ablation technique for creating complete cell death: irreversible electroporation. Radiology. May; 2010 255(2):426–33. [PubMed: 20413755]

11. Gilbert JC, Onik GM, Hoddick WK, Rubinsky B. Real time ultrasonic monitoring of hepatic cryosurgery. Cryobiology. Aug; 1985 22(4):319–30. [PubMed: 3896654]

12. De Poorter J, De Wagter C, De Deene Y, Thomsen C, Ståhlberg F, Achten E. Noninvasive MRI thermometry with the proton resonance frequency (PRF) method: in vivo results in human muscle. Magnetic resonance in medicine: official journal of the Society of Magnetic Resonance in Medicine/Society of Magnetic Resonance in Medicine. Jan; 1995 33(1):74–81.

13. Ahrar, Kamran, Ahrar, Judy U., Javadi, Sanaz, Pan, Li, Milton, Denái R., Wood, Christopher G., Matin, Surena F., Jason Stafford, R. Real-time magnetic resonance imaging-guided cryoablation of small renal tumors at 1.5 T. Invest Radiol. Jun; 2013 48(6):437–444. [PubMed: 23511191]

14. Silverman SG, Tuncali K, Adams DF, VanSonnenberg E, Zou KH, Kacher DF, Morrison PR, Jolesz FA. MR imaging-guided percutaneous cryotherapy of liver tumors: initial experience. Radiology. Dec; 2000 217(3):657–64. [PubMed: 11110925]

15. Harada J, Dohi M, Mogami T, Fukuda K, Miki K, Furuta N, Kishimoto K, Simizu T, Miyasaka K. Initial experience of percutaneous renal cryosurgery under the guidance of a horizontal open MRI system. Radiation medicine. Jan; 2001 19(6):291–6. [PubMed: 11837579]

16. Dohi, Michiko, Harada, Junta, Mogami, Takuji, Fukuda, Kunihiko, Toyama, Yoichi, Kashiwagi, Hideyuki. MR-guided percutaneous cryotherapy of malignant liver tumor under horizontal-magnetic open system: initial experience. Journal of hepato-biliary-pancreatic surgery. Jan; 2003 10(5):360–5. [PubMed: 14598136]

17. Mala T, Edwin B, Samset E, Gladhaug I, Hol PK, Fosse E, Mathisen O, Bergan A, Søreide O. Magnetic-resonance-guided percutaneous cryoablation of hepatic tumours. The European journal of surgery = Acta chirurgica. Aug; 2001 167(8):610–7. [PubMed: 11716448]

18. Hushek, Stephen G., Martin, Alastair J., Steckner, Michael, Bosak, Elyakim, Debbins, Josef, Kucharzyk, Walter. MR systems for MRI-guided interventions. Journal of magnetic resonance imaging: JMRI. Feb; 2008 27(2):253–66. [PubMed: 18219680]

19. Chinzei, Kiyoyuki, Hata, Nobuhiko, Jolesz, Ferenc A., Kikinis, Ron. MR Compatible Surgical Assist Robot: System Integration and Preliminary Feasibility Study. Feb.2001 (2000):1–10.

20. Hata, Nobuhiko, Tokuda, Junichi, Hurwitz, Shelley, Morikawa, Shigehiro. MRI-compatible manipulator with remote-center-of-motion control. Journal of magnetic resonance imaging: JMRI. May; 2008 27(5):1130–8. [PubMed: 18407542]

21. Christoforou, Eftychios, Akbudak, Erbil, Ozcan, Alpay, Karanikolas, Menelaos, Tsekos, Nikolaos V. Performance of interventions with manipulator-driven real-time MR guidance: implementation and initial in vitro tests. Magnetic resonance imaging. Jan; 2007 25(1):69–77. [PubMed: 17222717]

22. Melzer, Andreas, Gutmann, Bernd, Remmele, Thomas, Wolf, Renate, Lukoscheck, Andreas, Bock, Michael, Bardenheuer, Hubert, Fischer, Harald. INNOMOTION for percutaneous image-guided interventions: principles and evaluation of this MR- and CT-compatible robotic system. IEEE engineering in medicine and biology magazine: the quarterly magazine of the Engineering in Medicine & Biology Society. Jan; 2008 27(3):66–73.

23. Bricault, Ivan, Zemiti, Nabil, Jouniaux, Emilie, Fouard, Céline, Taillant, Elise, Dorandeu, Frederic, Cinquin, Philippe. Light puncture robot for CT and MRI interventions: designing a new robotic architecture to perform abdominal and thoracic punctures. IEEE engineering in medicine and biology magazine: the quarterly magazine of the Engineering in Medicine & Biology Society. Jan; 2008 27(3):42–50.

24. Wu, Faye Y., Torabi, Meysam, Yamada, Atsushi, Golden, Alex, Fischer, Gregory S., Tuncali, Kemal, Frey, Dan D., Walsh, Conor. An MRI Coil-Mounted Multi-Probe Robotic Positioner for Cryoablation. Volume 6A: 37th Mechanisms and Robotics Conference; aug 2013; ASME; page V06AT07A012

25. Hata, Nobuhiko, Song, Sang-Eun, Olubiyi, Olutayo, Arimitsu, Yasumichi, Fujimoto, Kosuke, Kato, Takahisa, Tuncali, Kemal, Tani, Soichiro, Tokuda, Junichi. Body-mounted robotic instrument guide for image-guided cryotherapy of renal cancer. Medical physics. Feb; 2016 43(2):843–53. [PubMed: 26843245]

26. Arnolli, Maarten M., Hanumara, Nevan C., Franken, Michel, Brouwer, Dannis M., Broeders, Ivo AMJ. An overview of systems for CT- and MRI-guided percutaneous needle placement in the thorax and abdomen. The international journal of medical robotics + computer assisted surgery: MRCAS. Dec.2014

27. Tokuda, Junichi, Fischer, Gregory S., Papademetris, Xenophon, Yaniv, Ziv, Ibanez, Luis, Cheng, Patrick, Liu, Haiying, Blevins, Jack, Arata, Jumpei, Golby, Alexandra J., Kapur, Tina, Pieper, Steve, Burdette, Everette C., Fichtinger, Gabor, Tempany, Clare M., Hata, Nobuhiko. OpenIGTLink: an open network protocol for image-guided therapy environment. Int J Med Robot. Dec; 2009 5(4):423–34. [PubMed: 19621334]

28. Bidgood WD, Horii SC, Prior FW, Van Syckle DE. Understanding and using DICOM, the data interchange standard for biomedical imaging. Journal of the American Medical Informatics Association: JAMIA. 1997; 4(3):199–212. [PubMed: 9147339]

29. Gering DT, Nabavi A, Kikinis R, Hata N, O'Donnell LJ, Grimson WE, Jolesz FA, Black PM, Wells WM 3rd. An integrated visualization system for surgical planning and guidance using image fusion and an open MR. J Magn Reson Imaging. 2001; 13(6):967–975. [PubMed: 11382961]

30. Fedorov, Andriy, Beichel, Reinhard, Kalpathy-Cramer, Jayashree, Finet, Julien, Fillion-Robin, Jean-Christophe C., Pujol, Sonia, Bauer, Christian, Jennings, Dominique, Fennessy, Fiona, Sonka, Milan, Buatti, John, Aylward, Stephen, Miller, James V., Pieper, Steve, Kikinis, Ron. 3D Slicer as an image computing platform for the Quantitative Imaging Network. Magnetic resonance imaging. Nov; 2012 30(9):1323–41. [PubMed: 22770690]

31. Frangi, AF., Niessen, WJ., Vincken, KL., Viergever, MA. Multiscale vessel enhancement filtering. In: Wells, WM.Colchester, A., Delp, S., editors. Medical Image Computing and Computer-Assisted Intervention (MICCAI'98), Lecture Notes in Computer Science. Springer Verlag; 1998. p. 130-137.

32. Duda RO, Hart PE. Use of the Hough Transformation to Detect Lines and Curves in Pictures. Comm ACM. 1972; 15:11–15.

33. Antiga L. Generalizing vesselness with respect to dimensionality and shape. The Insight Journal. 2007

34. Mosaliganti K, Gelas A, Cowgill P, Megason S. An Optimized N-Dimensional Hough Filter for Detecting Spherical Image Objects. Insight Journal. 2009

35. Lorensen WE, Cline HE. Marching Cubes: A high resolution 3D surface construction algorithm. Computer Graphics. 1987; 21(4):163–169.

36. Johnson HJ, Harris G, Williams K. BRAINSFit: Mutual Information Registrations of Whole-Brain 3D Images, Using the Insight Toolkit. The Insight Journal. 2007

37. Kubota, Yoshiki, Matsumura, Akihiko, Fukahori, Mai, Minohara, Shin-Ichi, Yasuda, Shigeo, Nagahashi, Hiroshi. A new method for tracking organ motion on diagnostic ultrasound images. Med Phys. Sep.2014 41(9):092901. [PubMed: 25186417]

38. Chang, Kai-Hsiang, Ho, Ming-Chih, Yeh, Chi-Chuan, Chen, Yu-Chien, Lian, Feng-Li, Lin, Win-Li, Yen, Jia-Yush, Chen, Yung-Yaw. Effectiveness of external respiratory surrogates for in vivo liver motion estimation. Med Phys. Aug; 2012 39(8):5293–5301. [PubMed: 22894455]

39. Preiswerk, Frank, Toews, Matthew, Cheng, Cheng-Chieh, Chiou, Yuan George, Jr, Mei, Chang-Sheng, Schaefer, Lena F., Scott Hoge, W., Schwartz, Benjamin M., Panych, Lawrence P., Madore, Bruno. Hybrid MRI-Ultrasound acquisitions, and scannerless real-time imaging. Magn Reson Med. Oct 13.2016

40. Krieger, Axel, Susil, Robert C., Ménard, Cynthia, Coleman, Jonathan a, Fichtinger, Gabor, Atalar, Ergin, Whitcomb, Louis L., Member, Senior. Design of a novel MRI compatible manipulator for image guided prostate interventions. IEEE Trans Biomed Eng. Feb; 2005 52(2):306–313. [PubMed: 15709668]

41. De Oliveira, Jaane Rauschenberg, Beyersdorff, Dirk, Semmler, Wolfhard, Bock, Michael, de Oliveira, André. Automatic passive tracking of an endorectal prostate biopsy device using phase-only cross-correlation. Magn Reson Med. May; 2008 59(5):1043–1050. [PubMed: 18429016]

Appendix

In this study, the center of the circle that is fitted to the detected markers was estimated by the intersection of the perpendicular bisectors of two chords defined by three different points

on the circle (Figure 9). Given three markers selected from the detected markers, P_1, P_2 and P_3, the bisecting point of P_1P_2 and P_2P_3, represented by M_{12} and M_{23} can be obtained by:

$$m_{12} = \frac{(p_1 + p_2)}{2}, \quad (7)$$

$$m_{23} = \frac{(p_2 + p_3)}{2}, \quad (8)$$

where p_1, p_2, p_3, m_{12}, and m_{23} are the 2-dimensional position vectors of P_1, P_2, P_3, M_{12} and M_{23}. The unit normal vectors for the perpendicular bisectors of P_1P_2 and P_2P_3:

$$n_{12} = R_{90°}v_{12}, \quad (9)$$

$$n_{23} = R_{90°}v_{23}, \quad (10)$$

where $v_{12} = p_2 - p_1$ and $v_{23} = p_3 - p_2$, and $R_{90°}$ is a counter-clockwise rotation about the origin by 90 degrees.

The projection of M_{12} onto the perpendicular bisector of P_1P_2, represented by H_{12} is calculated by:

$$h_{12} = m_{12} + \{(m_{23} - m_{12}) \cdot n_{12}\}n_{12}. \quad (11)$$

The intersection of the two perpendicular bisectors, C, can be represented using a scalar parameter a:

$$c = m_{23} + an_{23}. \quad (12)$$

Since the projection of C onto M_2H must be H:

$$an_{23} \cdot \frac{(h_{12} - m_{23})}{\|h_{12} - m_{23}\|} = \|h_{12} - m_{23}\|. \quad (13)$$

Using this relationship, the scalar parameter a can be calculated as:

$$a = \frac{\|\boldsymbol{h}_{12} - \boldsymbol{m}_{23}\|^2}{\boldsymbol{n}_{23} \cdot (\boldsymbol{h}_{12} - \boldsymbol{m}_{23})}. \quad (14)$$

Therefore,

$$c = \boldsymbol{m}_{23} + \boldsymbol{n}_{23} \frac{\|\boldsymbol{h}_{12} - \boldsymbol{m}_{23}\|^2}{\boldsymbol{n}_{23} \cdot (\boldsymbol{h}_{12} - \boldsymbol{m}_{23})}. \quad (15)$$
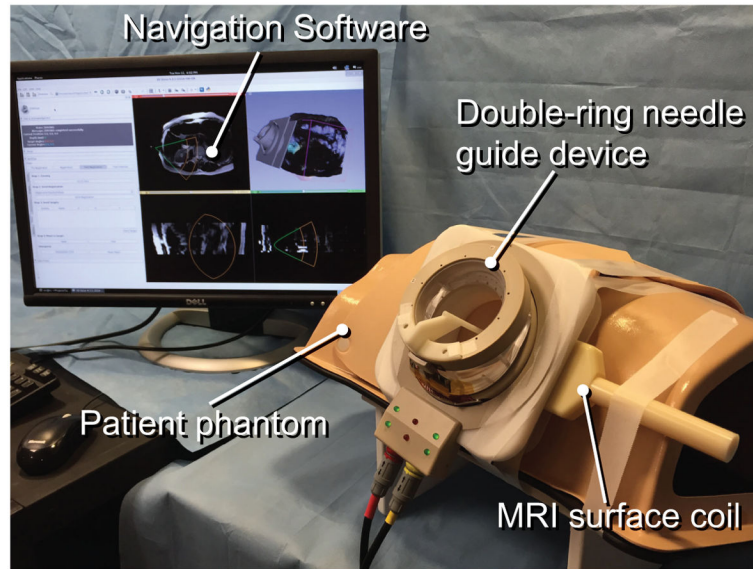
Figure 1.
The double-ring needle guide device is set up on a patient body phantom with an MRI-surface coil. The graphical user interface of the navigation software is shown on the display.
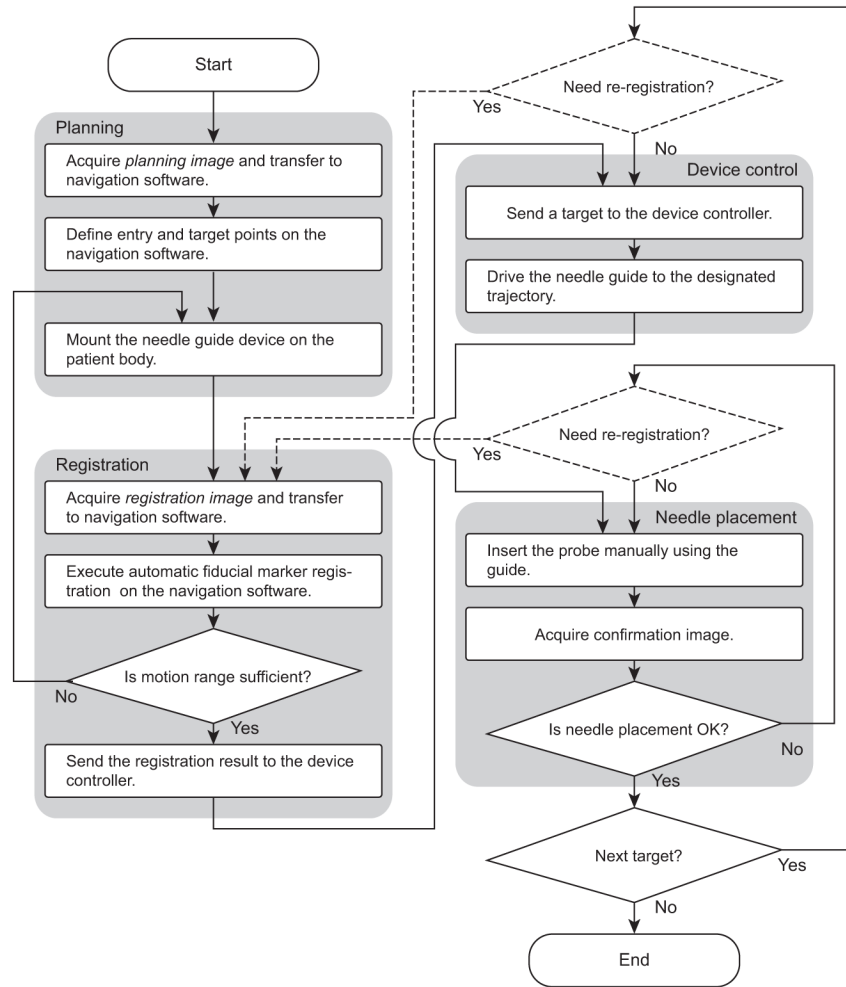
Figure 2.
Clinical workflow of MRI-guided percutaneous cryoablation using the proposed patient-mounted needle guide system. When the motion compensation technique is used, the device is re-registered each confirmation image to update the plan (indicated with broken lines).
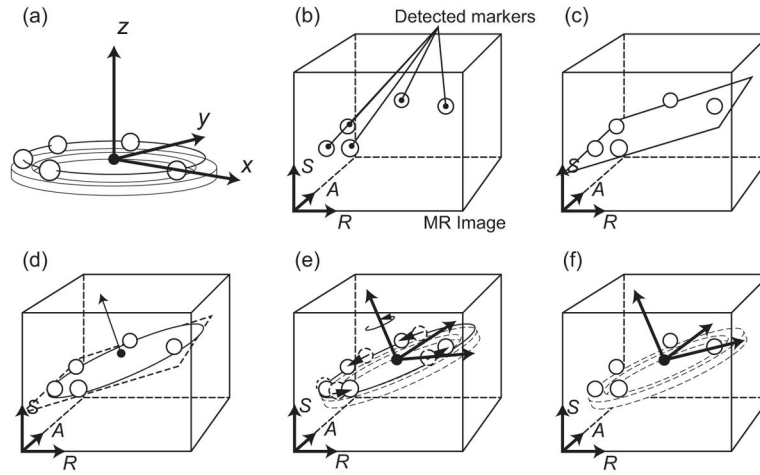
Figure 3.
Steps of automatic fiducial registration are shown. (a) The configuration of fiducial frame with multiple MR-visible markers aligned in a circle. The origin of the fiducial coordinate system is at the center of the circle, and the *x*-axis is defined by the line from the origin to the first marker. The *z*-axis is perpendicular to the circle. (b) The markers are detected as spherical objects in an MR image and encoded using the image coordinate system (right-anterior-superior or RAS). (c) A plane is fitted to the detected markers using an principal component analysis. (d) A circle that fit the detected markers is determined. (e) The fiducial frame is rotated about the *z*-axis to minimize the distances between the closest pairs. (f) The transform that registers the fiducial frame to the detected markers is determined.
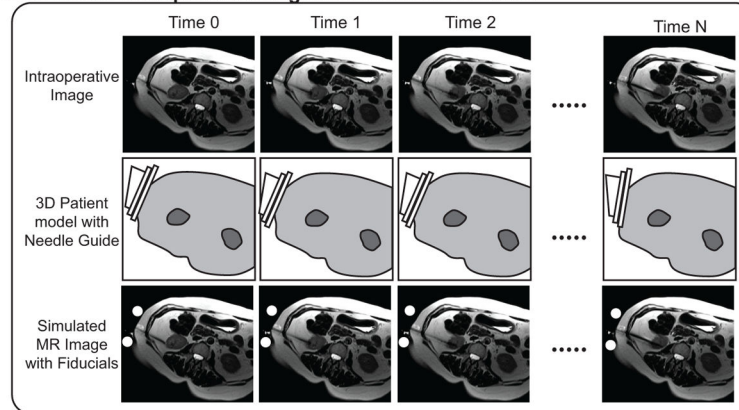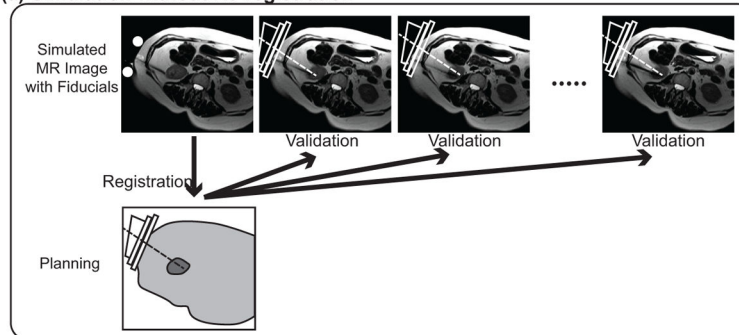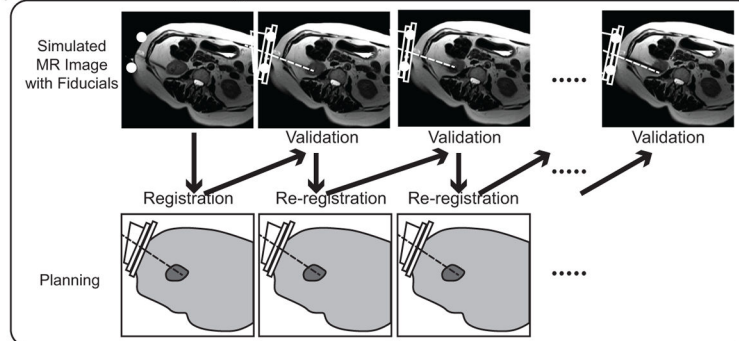
Figure 4.
A schematic representation of the simulation of needle guidance using intraprocedural MR images acquired during conventional MR-guided renal cryoablation.
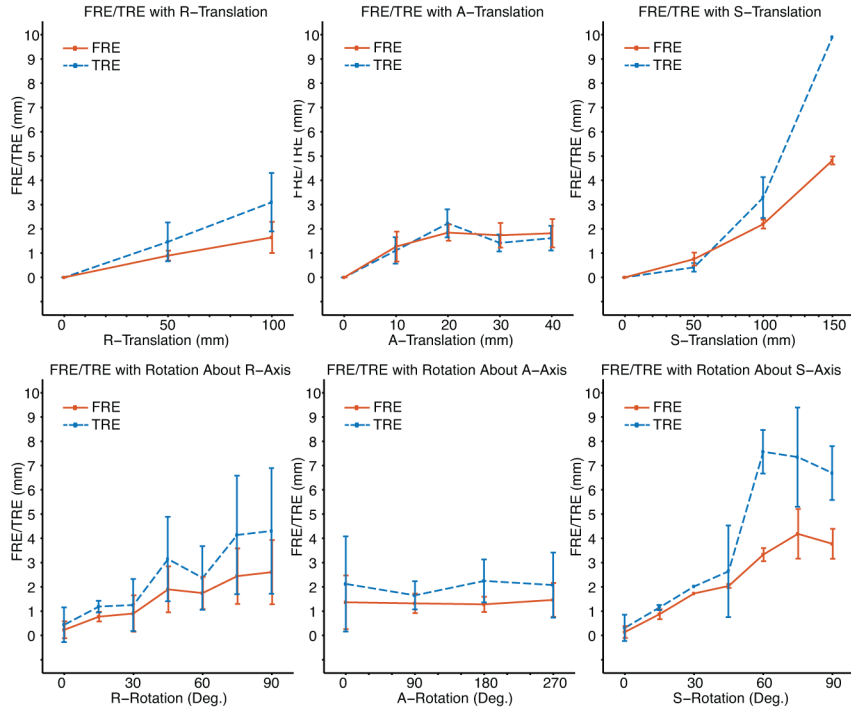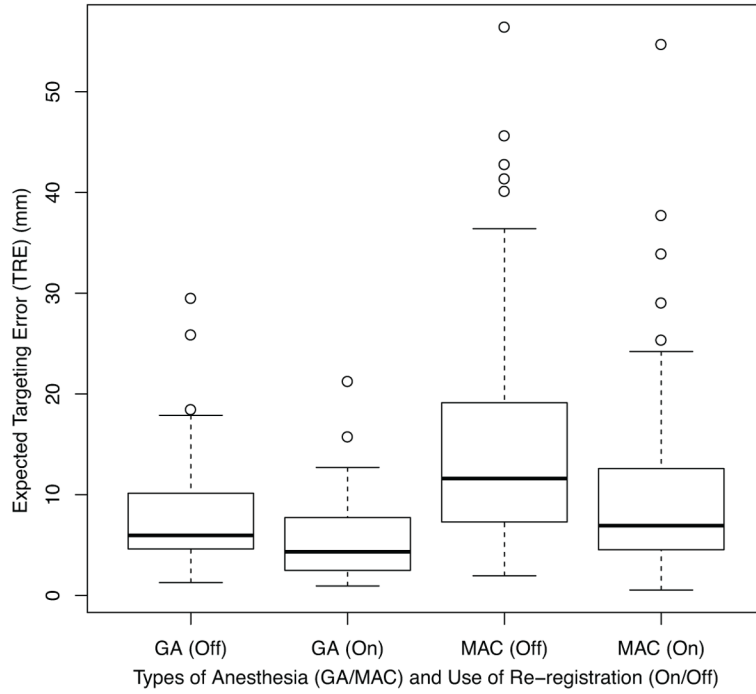
Figure 5.
FRE and TRE resulted in the imaging experiment were evaluated with varying translation of the fiducial frame from the initial position (isocenter) along the right-left (*R*-), anterior-posterior (*A*-), and superior-inferior (*S*-) axes, as well as rotation about the *R*-, *A*-, and *S*-axes.
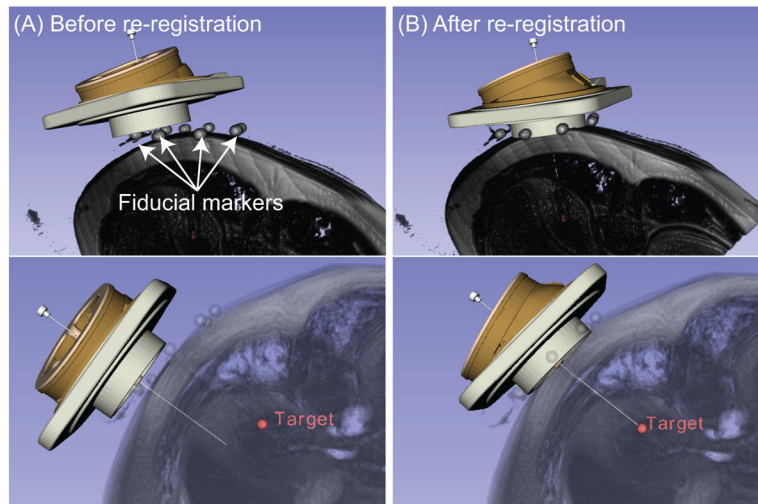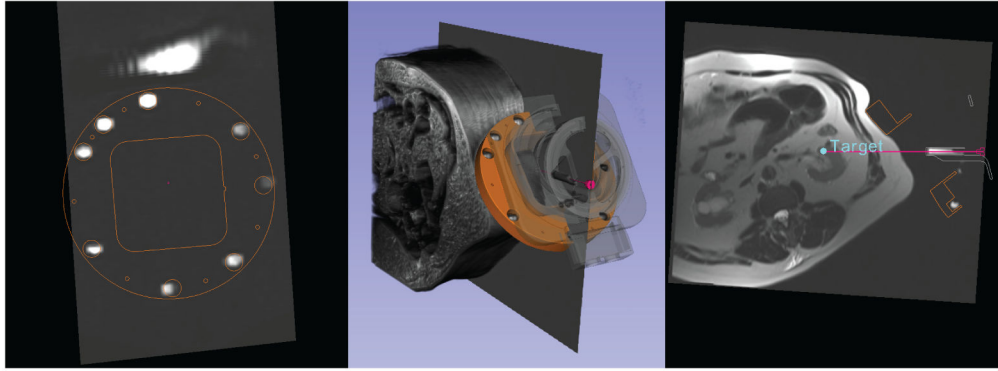
Figure 6.
A 3D model of the needle guide device is overlaid onto the volume rendering of an intraprocedural MR image with the simulated fiducial markers before (A) and after (B) re-registration. The presented image was acquired 32 minutes after the acquisition of the baseline image. The device was initially registered to the baseline image, and then re-registered to the presented image. The simulated fiducial markers were rendered at the locations estimated based on the entry point of the needle, and the orientation of the skin surface around it. The image with the fiducial markers was then used as an input for the re-registration. While there is a significant offset between the potential needle trajectory and the target before the re-registration, re-registration of the model could reduce the offset.
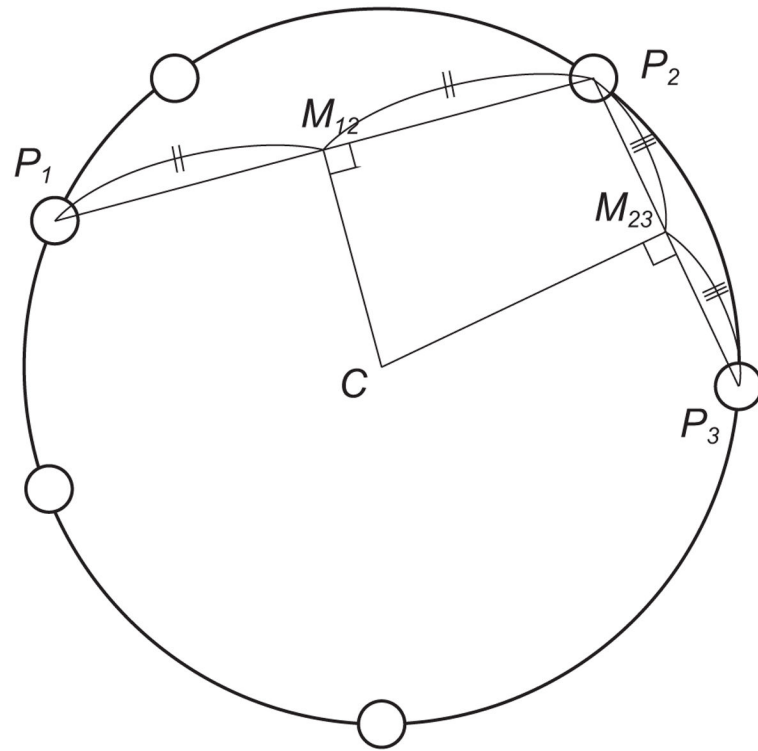
Figure 7.
Expected targeting error (ETE) based on the retrospective analysis of MR images acquired 20 kidney cancer patients treated by MRI-guided cryoablation. ETEs were estimated with and without re-registration of the needle guide on each needle confirmation image for patient group treated under free-breathing condition using monitored anesthesia care (MAC) ($n = 12$) and group treated under controlled breathing condition using general anesthesia (GA) ($n = 8$). The ETEs estimated without and with re-registration were compared using a paired Wilcoxon rank sum test. In both groups, the ETEs with re-registration were significantly lower than the ETEs without re-registration ($p < 0.005$ for GA and $p < 1.0 \times 10^{-5}$ for MAC).

Figure 8.

A result of device-to-image registration confirmed by overlying a model of the registered fiducial markers (orange line) and the registration image (left), 3D rendering of the patient and registered 3D model of the needle guide device (middle), and expected trajectory of the needle after directing the needle guide to the target based on the registration result (right).

Figure 9.
The schematic image shows our approach to estimate the center of the circular fiducial frame based on three detected markers. In our registration algorithm, the center was estimated based on all conventions of three markers.